RSC Advances

This article can be cited before page numbers have been issued, to do this please use: W. Guo, X. Ma, X. Zhang, Y. Zhang, D. Yu and X. He, *RSC Adv.*, 2016, DOI: 10.1039/C6RA16337H.

ROYAL SOCIETY OF CHEMISTRY

www.rsc.org/advances

View Article Online
DOI: 10.1039/C6RA16337H

Spinel $CoMn_2O_4$ Nanoparticles Supported on Nitrogen and Phosphorus Dual Doped Graphene Aerogel as Efficient Electrocatalysts for the Oxygen Reduction Reaction

Wenhui Guo,[a] Xiuxiu Ma,[a] Xianlei Zhang,[a] Yaqing Zhang,[a] Dingling Yu,[a] Xingquan He,*[a]

[a]*Department of Chemistry and Chemical Engineering, Changchun University of Science and Technology, Changchun 130022, P. R. China.*

* Corresponding author. Tel.+86-431-85583430
E-mail address:hexingquan@hotmail.com (Xingquan He);

View Article Online
DOI: 10.1039/C6RA16337H

Abstract

In this work, we present a novel hybrid composed of spinel $CoMn_2O_4$ nanoparticles and N, P dual-doped graphene aerogel ($CoMn_2O_4$/NPGA). The $CoMn_2O_4$/NPGA is characterized by scanning electron microscopy (SEM), transmission electron microscopy (TEM), X-ray diffraction (XRD), Thermogravimetric analysis (TGA), Raman spectroscopy, and X-ray photoelectron spectroscopy (XPS), respectively. The electrocatalytic activity of the $CoMn_2O_4$/NPGA composite towards the ORR was assessed using linear sweep voltammetry method. Rotating disk electrode (RDE) measurements expose that the as-obtained $CoMn_2O_4$/NPGA shows an excellent ORR activity in an alkaline medium comparable to the benchmark Pt/C catalyst. Electrochemical measurements reveal that the ORR on $CoMn_2O_4$/NPGA proceeds through an almost four-electron pathway. Simultaneously, the methanol tolerance and operational stability of $CoMn_2O_4$/NPGA toward ORR are prominently higher than those of commercial Pt/C. All these conspicuous properties suggest that our proposed $CoMn_2O_4$/NPGA may be used as a prospective Pt-free catalyst in alkaline direct methanol fuel cells.

Keywords: N, P dual-doped graphene aerogel; $CoMn_2O_4$ nanoparticles; hydrothermal reaction; oxygen reduction reaction

1. Introduction

The oxygen reduction reaction (ORR) is vital in electrochemical energy storage and conversion technologies including fuel cells and metal−air batteries. Nevertheless, the ORR process is subjected to sluggish kinetics, and thus electrocatalysts for the ORR are the key part in these fields.[1-5] Pt or its alloys are the best known ORR catalysts.

View Article Online
DOI: 10.1039/C6RA16337H

However, the sluggish ORR kinetics, crossover effects, poor stability in long-term operation, as well as the high price, have restricted their utilizations.

Until now, electrocatalysts based on nonprecious metal oxides have been vastly investigated. The first row transition metal (Mn, Fe, Co, Ni, Cu etc.) oxides have especially attracted tremendous attention because of their outstanding ORR activity, prominent stability and low cost.[6-16] Among these oxides, mixed-valence transition-metal oxides with a spinel structure (general formula AB_2O_4) have proven to possess the reinforced electrochemical properties from single metal oxides for the ORR.[9,17] However, they have accomplished little success in the recent state of investigation and development because of their poor electrical conductivity.

Hence spinel oxides are usually supported on conducting carbon (carbon nanotubes, graphene and carbon black, etc) to guarantee excellent conductivity. Among these carbon materials, graphene, a unique sp^2-hybridized carbon, is the most hopeful carbon support. Large specific surface area, high electronic conductivity, high chemical stability and light weight make graphene a perfect terrace for anchoring or growing nanomaterials.[18-21] In particular, modification of graphene by the heteroatom (e.g., N, S, B, or P) doped is possibly great to enhance catalytic activity with more active reactive sites and higher electron transfer rate.[22-25] Therefore, heteroatom-doped graphene supported spinel hybrid materials were synthesized and displayed an excellent performance towards the ORR.[26, 27] In addition to the heteroatom doping, high electrical conductivity can also be obtained from hierarchical structures. Hierarchical structures can provide adequate passageways to

View Article Online
DOI: 10.1039/C6RA16337H

guarantee the electron transfer and diffusion of electrolyte.[28–32] We speculate that the combination of spinel oxides with heteroatom doped hierarchical structures will lead to high electrocatalytic performance of the obtained hybrids.

Herein, we present a novel hybrid composed of $CoMn_2O_4$ spinel nanoparticles and three-dimensional N, P dual-doped graphene aerogel ($CoMn_2O_4$/NPGA). The obtained $CoMn_2O_4$/NPGA composite material is an efficient ORR catalyst with high catalytic activity in an alkaline medium comparable to the benchmark Pt/C catalyst, and displays better methanol tolerance and durability than Pt/C. The superior performance makes it a likely catalyst for the ORR in alkaline fuel cells.

2. Experimental section

2.1. Materials and reagents

Graphite powder was purchased from Sinopharm Chemical Reagent Co., Ltd. Pt/C (20 wt% Pt on Vulcan XC-72) was purchased from Alfa Aesar. Hypophosphorous acid was bought from Sinopharm Chemical Reagent Co., Ltd. Nafion (5%) was purchased from Sigma-Aldrich. All other reagents were of analytical grade and used without further purification, including ethanol, $NaNO_3$, $KMnO_4$, H_2O_2, KOH, $MnCl_2{\cdot}4H_2O$, $CoCl_2{\cdot}6H_2O$， urea and D-glucose. Ultra pure water was obtained from a Milli-Q water system (18.2 MΩ cm).

2.2. Synthesis of manganese dioxide noparticle (MnO_2)

Manganese dioxide nanoparticles (MnO_2) were synthesized according to the method described in the literature.[33] Simply, $MnCl_2{\cdot}4H_2O$ (0.003 mol) was dispersed in 100 ml ultra pure water under vigorous stirring. $KMnO_4$ (0.002 mol) was added into 50ml

View Article Online
DOI: 10.1039/C6RA16337H

KOH aqueous solution (pH=12), and then the solution was transferred into the above $MnCl_2 \cdot 4H_2O$ solution with stirring at room temperature. The obtained suspension was continuously stirred at room temperature for 3 h. Finally, the formed brown precipitate was filtered, washed with distilled water and absolute ethanol, and dried overnight at 60 ºC.

2.3. Synthesis of $CoMn_2O_4$/nitrogen phosphorus dual doped graphene aerogel ($CoMn_2O_4$/NPGA)

The graphite oxide (GO) was gained from the natural graphite by a modified Hummers' method.[34, 35] MnO_2 (0.01 g), GO (2 mg ml^{-1}, 10 ml), urea (1 g), and D-glucose (0.04 g) were decentralized by ultrasonic vibration for 25 min (Scheme 1A) and then sealed in a Teflon lined stainless-steel autoclave. The autoclave was kept at 180 ºC for 12 h, and then cooled to room temperature spontaneously. (Scheme 1B) After freeze-drying for 10 h, the obtained MnO_2/nitrogen doped graphene aerogel (MnO_2/NGA) was dipped into $CoCl_2 \cdot 6H_2O$ solution (0.2 g, 5 ml) for three days. Following, the product was put in 10 ml of 4 mol L^{-1} KOH aqueous solution containing 2.5 ml hypophosphorous acid (the volume ratio of hypophosphorous acid to water is 1:1) for one day before freeze-drying. (Scheme 1C) For control experimentation, nitrogen-doped graphene aerogel (NGA), and nitrogen and phosphorus co-doped graphene aerogel (NPGA) were also fabricated through the same procedure as $CoMn_2O_4$/NPGA except for adding MnO_2, cobalt salt and hypophosphorous acid, and MnO_2 and cobalt salt, respectively.

2.4. Preparation of modified electrode

View Article Online
DOI: 10.1039/C6RA16337H

Before modification, the working electrode was polished with 1.0, 0.3 and 0.05 μm aluminum oxide powder, respectively, then sonicated in distilled water, ethanol and distilled water in turn. Afterwards, the cleaned glassy carbon (GC) electrode was blow-dried with N_2 at room temperature. The modification of the working electrode was achieved using the drop-dry method. 1.0 mg $CoMn_2O_4$/NPGA and 1.0 mL ethanol were mixed ultrasonically to obtain a uniform ink. A certain amount of the catalyst ink at a concentration of 1 mg mL^{-1} was cast on the GC disk and left to dry. The catalyst loading per area on the GC electrode was kept to be 280 μg cm^{-2}. The same amount of the NGA, NPGA, MnO_2/NGA or Pt/C (20 wt%) catalyst was also loaded onto a GC electrode for comparison.

2.5. Characterization

The morphologies and structures of the fabricated samples were acquired under scanning electron microscopy (SEM, JEOL JSM-6701F electron microscope operating at 5 kV), transmission electron microsopy (TEM, tecnai G220 S-Twin transmission electron microscope operating at 200 kV) and X-ray diffractometer (RIGAK, D/MAX2550 VB/PC, Japan). Thermogravimetric analysis (TGA) was carried out with Pyris Diamond analyzer. The specimens were heated in a temperature range from ambient temperature to 900 ºC in air with a heating rate of 10 ºC min^{-1}. Raman spectra were operated on a TriVista^{TM}555CRS Raman spectrometer. The laser frequency used was the 532 nm line. Simulations were performed by using Peakfit software. X-ray photoelectron spectroscopy (XPS) measurements were performed using an ESCLAB 250 spectrometer with a monochromatized Al Kα X-ray source

View Article Online
DOI: 10.1039/C6RA16337H

(1486.6 eV photons) to determine surface chemical compositions and the bonding states. Fitting was done using a nonlinear least-squares curve-fitting program (XPSPEAK41 software). XPS deconvolution conditions showed that the background type was Shirley and the FWHM value, as well as the percentage Lorentzian–Gaussian value of these peaks split by the same peak should be close. The Brunauer–Emmett–Teller (BET) surface areas and pore volumes were evaluated using nitrogen adsorption–desorption isotherms measured on an ASAP2020 volumetric adsorption analyzer at 77 K.

2.6. Electrochemical measurements

Rotating disk electrode (RDE) and rotating ring disk electrode (RRDE) experiments were performed on a CHI 660E electrochemical workstation (CH Instruments, USA) in a conventional three electrode cell using the coated GC electrode as the working electrode, a platinum wire as the auxiliary electrode, and a saturated calomel electrode (SCE) as reference. Linear sweep voltammetry (LSV) and long-term chronoamperometric measurements were performed at a GC rotating disk electrode (d=5 mm). LSV measurements were carried out in N_2 or O_2-saturated solution at rotation speeds varying from 200 to 2500 rpm and with a scan rate of 10 mV s^{-1}. Chronoamperometric durability experiments were performed at a constant potential of -0.4 V vs. SCE in an O_2-saturated solution with a rotation speed of 1600 rpm. RRDE (d_{disk} =5.61 mm) experiments were performed using a Pine Instrument Company AF-MSRCE and a platinum ring, resulting in a collection efficiency of the Pt ring electrode, N = 37%. These experiments were performed at 1600 rpm in N_2 or

View Article Online
DOI: 10.1039/C6RA16337H

O_2-saturated KOH solution. The disk potential was swept at 10 mV s^{-1}. The Pt ring electrode was polarized at 0.5 V vs. SCE for oxidizing the hydrogen peroxide ion during oxygen reduction at the modified GC disk electrode. During the test, the trachea was put on the solution surface. All the experiments were carried out in N_2 or O_2-saturated 0.1 M KOH solution at room temperature.

3. Results and discussion

3.1. Characterization of the composite film

The morphologies and microstructures were enquired by the use of scan electron microscopy (SEM) and transmission electron microscopy (TEM). SEM images display that the NGA presented three-dimentional folded and wrinkled network architecture (Fig. 1a and b). For the as-synthesized $CoMn_2O_4$/NPGA, $CoMn_2O_4$ nanoparticles attached to the crumpled NPGA were clearly observed without obvious aggregation (Fig. 1c and d). Meanwhile, the EDS (Figure S1) suggested the presence of C, Co, Mn, O, P, and N components in the $CoMn_2O_4$/NPGA hybrid.

The TEM image reveals that the NGA presented a crumpled and wrinkle-like structure (Fig. 2a), which was consistent with the SEM result. For the NPGA, EDS indicated that the presence of C, N and P of the NPGA (Fig. S2). It indicated that N and P were successfully incorporated into graphene oxide. The size of $CoMn_2O_4$ nanoparticles supported on NPGA was in the range of 5–25 nm (Fig. 2b). The surface folding and wrinkling have been demonstrated to be advantageous for sensing and electrocatalytic applications because of lots of open edge sites.[36] The measured d spacing of $CoMn_2O_4$ nanoparticles was around 0.247 nm in the HRTEM image of

View Article Online
DOI: 10.1039/C6RA16337H

$CoMn_2O_4$/NPGA (Fig. 2c) corresponding to the (311) crystal plane of $CoMn_2O_4$.

Powder X-ray diffraction (XRD) was used to expose the crystalline nature of the obtained samples. The XRD profiles of the NGA, NPGA and $CoMn_2O_4$/NPGA are shown in Fig. 2 (d). All the characteristic peaks of the $CoMn_2O_4$/NPGA were readily indexed to $CoMn_2O_4$ phase in accordance with the standard values (JCPDS Card no. 818-0408), which suggested the formation of $CoMn_2O_4$ crystalline phase. Besides, a typical broad diffraction peak around 26º exposed that the interlayer spacing of NGA was smaller than that of GO (8.32 Å, 10.6°) but larger than that of graphite (3.36 Å, 26.5°), demonstrating the efficient reduction of graphene oxide.[37]

Fig. S3 shows a TGA curve of the $CoMn_2O_4$/NPGA up to 900 ºC at a heating rate of 10 ºC min^{-1}. TG curve showed that the total loading of $CoMn_2O_4$ was about 32.22%.

X-ray photoelectron spectroscopy (XPS) was employed to characterize electronic configurations of the atoms and the surface elemental compositions in the hybrid. Fig.3a presents the XPS survey spectra of NGA, MnO_2/NGA and $CoMn_2O_4$/NPGA, respectively. As expected, a full survey of $CoMn_2O_4$/NPGA showed peaks corresponding to the presence of P2p, Mn2p, Co2p, N1s, O1s, and C1s. The existence of phosphorus could be introduced by hypophosphorous acid (the reducing agent). The total phosphorus content was 1.22 at%. The high-resolution P2p spectrum (Figure 3b) was deconvoluted into three peaks located at 134.6, 133.45 and 133.1 eV, which should be attributed to C-O-PO_3, P-N and P-C bonding, respectively.[38, 39] The C-O-PO_3 bonding indicated that P was successfully bonded to carbon surface using one bridging oxygen bonding.[40] The formation of P–C confirmed that P atoms were

View Article Online
DOI: 10.1039/C6RA16337H

incorporated into the carbon framework. In high-resolution Mn2p XPS spectrum (Figure 3c), two peaks were observed at 641.5 and 652.91 eV, and other two peaks located at 643.01and 654.4 eV of $Mn2p_{3/2}$ and $Mn2p_{1/2}$ spin-orbit doublets deconvoluted peaks, which could be characterized to Mn^{2+} and Mn^{3+}, respectively.[41, 42] Above results indicated that the manganese in $CoMn_2O_4$/NPGA was Mn^{2+} and Mn^{3+} (Mn^{2+}/ Mn^{3+} ratio = 0.88, estimated from the corresponding peaks areas). Similarly, the high-resolution Co2p spectrum of $CoMn_2O_4$/NPGA (Fig. 3d) showed the peaks of $Co2p_{3/2}$ and $Co2p_{1/2}$. Co $2p_{3/2}$ spectrum exhibited components associated with Co^{3+} and Co^{2+} cations which were respectively centered at 780.9 and 782.2 eV. The satellite peaks located at 784.2 (Co^{2+}) and 788 eV (Co^{3+}) were two shake-up type peaks of the $Co2p_{3/2}$ edge.[43] The Co^{2+}/Co^{3+} ratio was estimated to be around 1.23 from their corresponding peak areas. The high-resolution N1s XPS spectra of $CoMn_2O_4$/NPGA are revealed in Fig. 3e. The total nitrogen content was as high as 2.35 at%. The N 1s peaks of $CoMn_2O_4$/NPGA clearly indicated that the peaks of nitrogen functionalities appeared at 400.10 eV (pyrrolic N) and 398.79 eV (pyridinic N). Relative surface concentrations of nitrogen and phosphorus species obtained by N1s high-resolution XPS and P2p high-resolution XPS spectra of $CoMn_2O_4$/NPGA were summarized in the Table S1.

Raman spectroscopy was used to characterize the structural information on the carbonaceous materials and in particular disorder and defect structures. Results obtained for NGA and $CoMn_2O_4$/NPGA in the spectral region of 900–1700 cm^{-1} are respectively presented in Fig. S4 (a) and (b). As a result of the fit, several parameters

View Article Online
DOI: 10.1039/C6RA16337H

were extracted and presented in Table S2. Our samples all had five bands located at ca. 1200 cm^{-1}, 1350 cm^{-1} (D mode), 1500 cm^{-1}, 1590 cm^{-1} (G mode) and 1620 cm^{-1} (D′ mode) respectively. Lorentzian line shapes were used for D and G bands, whereas Gaussian ones were used to simulate the D′ band as well as the bands centered at ca. 1200 cm^{-1} and 1500 cm^{-1}.[44] An upward shift of the G-band of $CoMn_2O_4$/NPGA (1591 cm^{-1}) could be observed with respect to the position of the G-band for the NGA (1585 cm^{-1}). This shift probably resulted from the high degree of disorder of $CoMn_2O_4$/NPGA. It is in fact well-known that the G band of disordered solids is shifted to higher Raman wave numbers than the G band of ordered ones.[45] The highly disordered character of $CoMn_2O_4$/NPGA was moreover in fair agreement with the observed D and G line widths of these two samples (Table S2). The increase in both line widths was an evidence for the decrease of the ordering degree for $CoMn_2O_4$/NPGA. I_D/I_G ratio allows evaluating the graphitization degree of a carbon-based material. The I_D/I_G is used as an indicator of the amount of defects in the carbon-based materials as well as to evaluate the in-plane crystallite size (L_a) which is a measure of the inter-defects distance. One of the relations describing the evolution of L_a with the integrated intensity ratio of G to D bands is the following one: L_a (nm) = $2.4\times10^{-10}\lambda^4_{laser} \times I_G/I_D$, in which λ_{laser} is the laser wavelength in nm.

From the L_a values calculated for $CoMn_2O_4$/NPGA and NGA, it was deduced that $CoMn_2O_4$/NPGA had lower crystallite size than NGA.

To investigate the porosity of the $CoMn_2O_4$/NPGA and the NGA, the N_2 sorption measurement was performed. The nitrogen adsorption–desorption curves categorized

View Article Online
DOI: 10.1039/C6RA16337H

as type IV isotherm, and a distinct hysteresis loop in the P/P° range of 0.5 to 1.0 (Fig. 4), which were strong indications of capillary condensation and multilayer adsorption.[46] The BET surface areas and pore volumes are summarized in Table 1. It is seen from Table 1 that the BET specific surface area and total pore volume for the $CoMn_2O_4$/NPGA were 135.8 m^2 g^{-1} and 0.302 cm^3 g^{-1}, respectively, which evidently decreased compared to the NGA due to the incorporation of the $CoMn_2O_4$ into NPGA. Both $CoMn_2O_4$/NPGA and NGA exhibited the existence of mesopores and macropores which provided effective triple phase (solide-liquide-gas) region for efficient mass transfer of O_2 and electrolyte.[47]

3.2. Electrochemical performance for ORR

In order to probe the ORR performance of $CoMn_2O_4$/NPGA, both rotating disk electrode (RDE) and rotating ring disk electrode (RRDE) measurements were carried out. Liner sweep voltammograms (LSVs) for the ORR on $CoMn_2O_4$/NPGA are displayed in Fig. 5 (a). LSVs on Pt/C, NPGA and NGA modified electrode are also given for comparison (Fig. 5 (b) and Fig. S5). It is seen from LSVs of the obtained samples, with increase of the rotation speed, the current density was enhanced obviously due to the shortened diffusion layer.[48] Apparently, the ORR onset potentials were kept almost immobile under different rotation speeds.

Fig. 5 (c) shows the RDE measurements obtained on $CoMn_2O_4$/NPGA, MnO_2/NGA, NGA, NPGA and Pt/C with the rotation rate of 1600 rpm in an O_2-saturated 0.1 M KOH solution, and the corresponding kinetics parameters for the ORR are summarized in Table 2. As seen from Table 2, the ORR onset potential of

View Article Online
DOI: 10.1039/C6RA16337H

$CoMn_2O_4$/NPGA commenced at about -0.094 V vs. SCE, which obviously shifted positively in comparison with those of MnO_2/NGA (-0.136 V vs. SCE), NGA (-0.147 V vs. SCE) and NPGA (-0.142 V vs. SCE), while was less positive than that of Pt/C (-0.028 V). The diffusion limiting current density on the $CoMn_2O_4$/NPGA was also found to be obviously larger than that on MnO_2/NGA, NGA and NPGA, and was close to that of Pt/C. Our $CoMn_2O_4$/NPGA catalyst was also compared with those spinel materials formerly reported in literatures (Table S3). It is noteworthy that the performance of our catalyst, including the onset potential and limiting current density, was close to or even better than those of previously reported spinel materials.

The Tafel curves of the ORR on the $CoMn_2O_4$/NPGA and Pt/C can be derived from the polarization curve of linear sweep voltammetry with a rotation speed of 1600 rpm, as shown in Fig. 5(d) .The $CoMn_2O_4$/NPGA and Pt/C catalysts exhibited the Tafel slopes of 77 and 78 mV $decade^{-1}$ at low overpotential, respectively, which implied the similar catalytic mechanism of ORR on the $CoMn_2O_4$/NPGA and Pt/C.

It is well known that the electrochemical reduction reaction of oxygen can occur via two primary possible pathways: including two electrons to produce H_2O_2 and HO_2^-, and the other, a direct transfer of four-electron pathway to produce H_2O and OH^- in acidic and alkaline media, respectively. In order to understand the ORR pathway on the $CoMn_2O_4$/NPGA electrode, RRDE experiments were performed. During the ORR process, the produced hydrogen peroxide species at the disk electrode can be detected by the ring electrode. The electron transfer number (n) and percentage of hydrogen peroxide ion ($\%HO_2^-$) on different catalysts can be

View Article Online
DOI: 10.1039/C6RA16337H

determined by the following equations.[49]

$$\%HO_2^- = \frac{200 \times I_R / N}{I_D + I_R / N} \quad (1)$$

$$n = \frac{4I_D}{I_D + I_R / N} \quad (2)$$

Where I_d is the disk current, I_r is the ring current, and N is the current collection efficiency of the Pt ring, which was determined to be 0.37.

Fig. 6 (a) presents the disk and ring current density for the $CoMn_2O_4$/NPGA and Pt/C catalysts in an O_2-saturated 0.1 M KOH solution. The yield of peroxide species (HO_2^-) and the electron transfer number (n) calculated based on the corresponding RRDE data are shown in Fig. 6 (b). The measured HO_2^- yield of the $CoMn_2O_4$/NPGA and Pt/C was 14.68-17.78% and 1.59-3.54% in the applied potential range from −0.35 to −0.6 V vs. SCE, respectively (based on Eq. (1)). The electron transfer number for the $CoMn_2O_4$/NPGA and Pt/C was 3.64-3.70 and 3.93-3.97 (calculated from Eq. (2)) at the given potentials from −0.35 to −0.6 V vs. SCE. The RRDE tests indicated that the $CoMn_2O_4$/NPGA resulted in an almost four-electron transfer pathway to produce OH^- for the ORR.

It is essential to estimate the stability of a new kind of electrocatalytic material using chronoamperometric durability measurements. The experiments were performed at a constant potential of −0.4 V vs. SCE in 0.1 M KOH solution saturated with O_2. As depicted in Fig. 7, the $CoMn_2O_4$/NPGA catalyst exhibited a much slower decay with a higher current retention (92.27%) after 10000 s, while only 80.18% of its initial current was retained for the commercial Pt/C catalyst under the same conditions.

View Article Online
DOI: 10.1039/C6RA16337H

These results implied that the $CoMn_2O_4$/NPGA catalyst possessed better stability than Pt/C.

Furthermore, for practical application in fuel cells, robust tolerance to methanol oxidation was a critical criterion for cathode electrocatalysts. On the matter, the tests on $CoMn_2O_4$/NPGA and Pt/C were performed in an O_2-saturated 0.1 M KOH solution with the addition of 3 M methanol in 300 seconds (Figure. 8). For the Pt/C, the catalytic activity deviated seriously due to its undesirable activity for methanol oxidation reaction (MOR) simultaneously occurring at the cathode. In contrast, when measured under the same conditions, the curve was no notable change of $CoMn_2O_4$/NPGA composite. These results indicated that the $CoMn_2O_4$/NPGA catalyst had better methanol-tolerance compared with Pt/C.

4. Conclusion

In conclusion, a novel $CoMn_2O_4$/NPGA composite with high catalytic activity towards the ORR was successfully fabricated from low-cost raw materials under mild conditions. The electrochemical measurements demonstrate that the $CoMn_2O_4$/NPGA composite exhibited more positive onset potential and amazingly high current density towards the ORR compared to NGA, which should be ascribed to P doping and the synergistic effect between $CoMn_2O_4$ and NPGA. The $CoMn_2O_4$/NPGA composite occupies high activity, good methanol tolerance and excellent durability, which may possess great promise as the ORR catalyst in alkaline DMFCs.

Acknowledgements

This work has been supported by the National Natural Science Foundation of China

View Article Online
DOI: 10.1039/C6RA16337H

under Grant No. 21273024, and Natural Science Foundation of Jilin Province, China under Grant No. 20160101298JC

References

1 B. Wang, J. *Power Sources*, 2005, **152**, 1-15.

2 Q. Tang, L. Jiang, J. Liu, S. Wang, G. Sun, *ACS Catal*., 2014, **4**, 457-463.

3 Z. Yang, H. Nie, X. Chen, X. Chen, S. Huang, *J. Power Sources*, 2013, **236**, 238-249.

4 J.-H. Jang, E. Lee, J. Park, G. Kim, S. Hong, Y.-U. Kwon, *Sci. Rep*., 2013, **3**, 2872.

5 M. Hamdani, R. N. Singh, P. Chartier, *Int. J. Electrochem. Sci*., 2010, **5**, 556-577.

6 J. Suntivich, H. A. Gasteiger, N. Yabuuchi, H. Nakanishi, J. B. Goodenough and S.-H.Yang, *Nat. Chem*., 2011, **3**, 546-550.

7 Y. Gorlin, B. Lassalle-Kaiser, J. D. Benck, S. Gul, S. M. Webb, V. K. Yachandra, J. Yano and T. F. Jaramillo, *J. Am. Chem. Soc*., 2013, **135**, 8525-8534.

8 Y. Y. Liang, Y. G. Li, H. L. Wang, J. G. Zhou, J. Wang, T. Regier and H. J. Dai, *Nature Mater.,* 2011, **10**, 780-786.

9 H. Zhu, S. Zhang, Y. X. Huang, L. Wu and S. Sun, *Nano letters*, 2013, **13**, 2947-2951.

10 B. Cao, G. M. Veith, J. C. Neuefeind, R. R. Adzic and P. G. Khalifah, *J. Am. Chem. Soc.*, 2013, **135**, 19186-19192.

11 I. Zaharieva, M. M. Najafpour, M. Wiechen, M. Haumann, P. Kurz and H. Dau, *Energy Environ. Sci*., 2011, **4**, 2400-2408.

12 T. Y. Ma, S. Dai, M. Jaroniec and S. Z. Qiao, *J. Am. Chem. Soc.*, 2014, **136**, 13925-13931.

View Article Online
DOI: 10.1039/C6RA16337H

13 W. G. Hardin, J. T. Mefford, D. A. Slanac, B. B. Patel,X. Q. Wang, S Dai, X. Zhao, R. S. Ruoff, K. P, Johnston and K. J. Stevenson, *Chem. Mater*., 2014, **26**, 3368-3376.

14 M. S. El-Deab and T. Ohsaka, *Angew. Chem., Int. Ed.*, 2006, **45**, 5963-5966.

15 K. Zhang, X. P. Han,Z. Hu, X. L. Zhang, Z. L. Tao and J. Chen, *Chem. Soc. Rev*., 2015, **44**, 699-728.

16 J. Kim, X. Yin, K. C. Tsao, S. Fang and H. Yang, *J. Am. Chem. Soc.*, 2014, **136**, 14646-14649.

17 C. C. Kuo, W. J. Lan and C. H. Chen, *Nanoscale*, 2014, **6**, 334-341.

18 A. K. Geim and K. S. Novoselov, *Nature Mater*., 2007, **6**, 183-191.

19 S. Yang, X. L. Feng, X. C. Wang and K. Müllen, *Angew. Chem., Int. Ed*., 2011, **50**, 5339-5343.

20 H. L. Wang, Y. Yang, Y. Y. Liang, J. T. Robinson, Y. G. Li, A. Jackson, Y. Cui and H. Dai, *Nano Lett.*, 2011, **11**, 2644-2647.

21 G. H. Yu, L. B. Hu, M. Vosgueritchian, H. L. Wang, X. Xie, J. R. McDonough, X. Cui, Y. Cui and Z. N. Bao, *Nano Lett*., 2011, **11**, 2905-2911.

22 R. Chen, J. Yan, Y. Liu and J. Li, *J. Phys. Chem. C*, 2015, **119**, 8032-8037.

23 S. Bag, B. Mondal, A. K. Das and C. R. Raj, *Electrochimica Acta*, 2015, **163**, 16-23.

24 R. Li, Z. D. Wei and X. L. Gou, *ACS Catal*., 2015, **5**, 4133-4142.

25 X. G. Duan, S. Indrawirawan, H. Q. Sun and S. B. Wang, *Catalysis Today*, 2015, **249**, 184-191.

26 R. Ning, J. Q. Tian, A. M. Asiri, A. H. Qusti, A. O. Al-Youbi and X. P. Sun, *Langmuir*, 2013, **29**, 13146-13151.

View Article Online
DOI: 10.1039/C6RA16337H

27 X. M. Ge, Y. Y. Liu, F. W. Goh, T. S. Hor, Y. Zong, P. Xiao, Z. Zhang, S. H. Lim, B. Li, X. Wang and Z. L. Liu, *ACS Appl. Mater. Interfaces*, 2014, **6**, 12684-12691.

28 Z. P. Chen, W. C. Ren, L. B. Gao, B. L. Liu, S, F, Pei and H. M. Cheng, *Nat. Mater.*, 2011, **10**, 424-428.

29 J. Liang, Y. Zheng, J. Chen, J. Liu, D. Hulicova-Jurcakova, M. Jaroniec and S. Z. Qiao, Angew. *Chem., Int. Ed.* 2012, **51**, 3892-3896.

30 Z. S. Wu, S. Yang, Y. Sun, K. Parvez, X. Feng and K. Mullen, *J. Am. Chem. Soc.*, 2012, **134**, 9082-9085.

31 F. Yavari, Z. Chen, A. V. Thomas, W. Ren, H. M. Cheng and N. Koratkar, *Sci. Rep.*, 2011, **1**, 166.

32 H. J. Yin, S. L. Zhao, J. W. Wan, H. J. Tang, L. Chang, L. C. He, H. J. Zhao, Y. Gao and Z. Y. Tang, *Adv. Mater.*, 2013, **25**, 6270-6276.

33 F. Y. Cheng, J. Shen, B. Peng, Y. D. Pan, Z. L. Tao and J. Chen, *Nature Chem*., 2011, **3**, 79-84.

34 W. S. Hummers and R. E. Offeman, *J. Am. Chem. Soc*., 1958, **80**, 1339-1339.

35 L. J. Cote, F. Kim and J. X. Huang, *J. Am. Chem. Soc*., 2009, **131**, 1043-1049.

36 C. C. Xu, Y. Su, D. J. Liu and X. Q. He, *Phys. C hem. Chem. P hys*., 2015, **17**, 25440-25448.

37 R. K. Huang, H. Ge, X. J. Lin, Y. L. Guo, R. S. Yuan, X. Z. Fu and Z. H. Li, *RSC Adv.*, 2013, **3**, 1235-1242.

38 R. Li, Z. D. Wei and X. L. Gou, *ACS Catal.*, 2015, **5**, 4133-4142.

39 F. Razmjooei, K. P. Singh, M. Y. Song amd J.-S. Yu, *Carbon*, 2014, **78**, 257-267.

View Article Online
DOI: 10.1039/C6RA16337H

40 X. X. Wu and L. R. Radovic, *Carbon*, 2006, **44**, 141-151.

41 N. Garg, M. Mishra, Govind and A. K. Ganguli, *RSC Adv*., 2015, **5**, 84988-84998.

42 S. G. Mohamed, Y. Q. Tsai, C. J. Chen, Y. T. Tsai, T. F. Hung, W. S. Chang and R. S. Liu, *ACS Appl. Mater. Interfaces*, 2015, **7**, 12038-12046.

43 I. Abidat, N. Bouchenafa-Saib, A. Habrioux, C. Comminges, C. Canaff, J. Rousseau, T. W. Napporn, D. Dambournet, O. Borkiewicz and K. B. Kokoh, *J. Mater. Chem*. *A*, 2015, **3**, 17433-17444.

44 J. W. Ma, A. Habrioux, Y. Luo, G. Ramos-Sanchez, L. Calvillo, G. Granozzi, P. B. Balbuena and N. Alonso-Vante, *J. Mater. Chem. A*, 2015, **3**, 11891-11904.

45 J. Ma, A. Habrioux, N. Guignard, and N. Alonso-Vante, *J. Phys. Chem. C*, 2012, **116**, 21788-21794.

46 D. U. Lee, B. J. Kim and Z. W. Chen, *Journal of Materials Chemistry A*, 2013, **1**, 4754-4762.

47 W. N. Yan, Z. R. Yang, W. Y. Bian and R. Z. Yang, *Carbon*, 2015, **92**, 74-83.

48 W. Yang, T.-P. Fellinger and M. Antonietti, *J. Am. Chem. Soc*., 2011, **133**, 206-209.

49 Y. Liu, Y. Y. Wu, G. J. Lv, T. Pu, X. Q. He and L. L. Cui, *Electrochim. Acta*, 2013, **112**, 269-278.

View Article Online
DOI: 10.1039/C6RA16337H

Figure captions

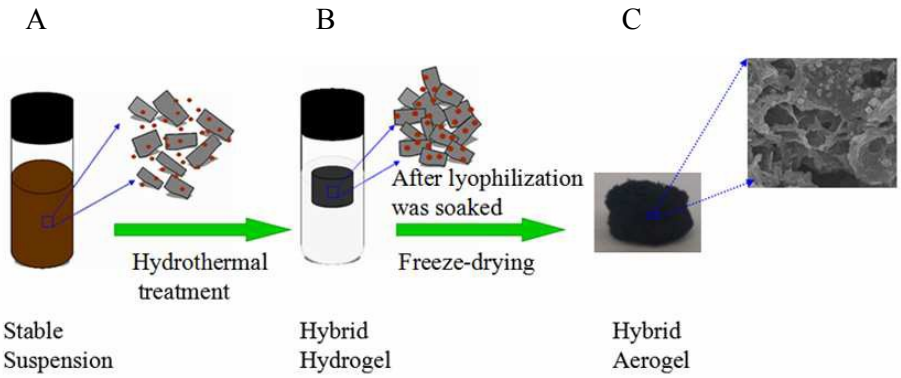

Scheme 1: Schematic illustration of the preparation of the $CoMn_2O_4$/NPGA. (A) Stable suspension of GO, MnO_2, D-glucose and urea dispersed in a vial. (B) 3D graphene hydrogel formed via a hydrothermal treatment. (C) The bulk aerogel of $CoMn_2O_4$/NPGA obtained after a freeze-drying process and its typical SEM image.

View Article Online
DOI: 10.1039/C6RA16337H

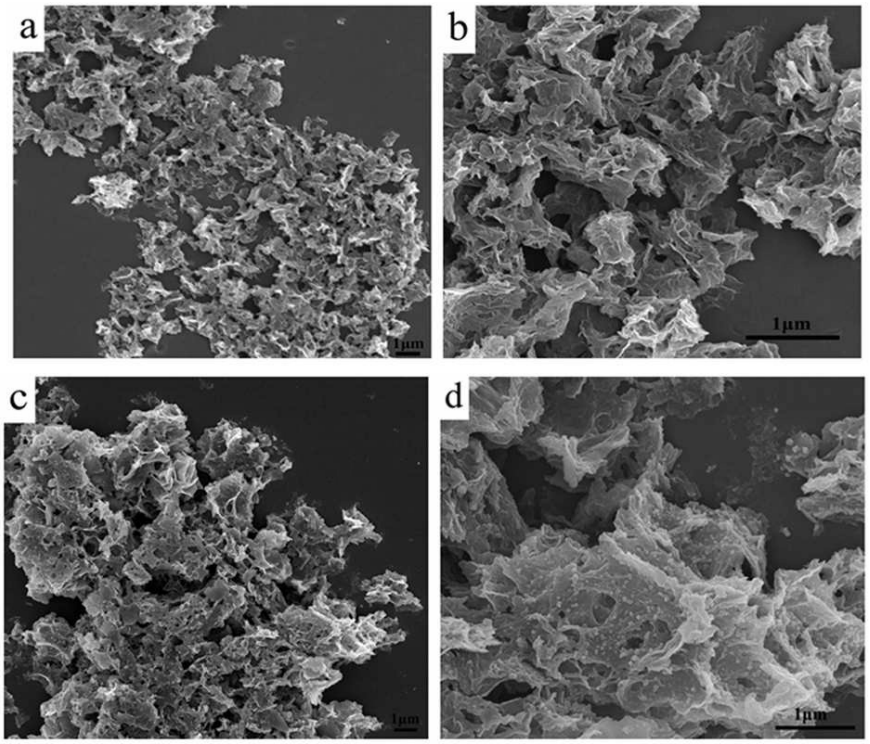

Fig. 1. SEM images of: (a, b) the NGA, (c, d) the $CoMn_2O_4$/NPGA composite at different magnifications.

View Article Online
DOI: 10.1039/C6RA16337H

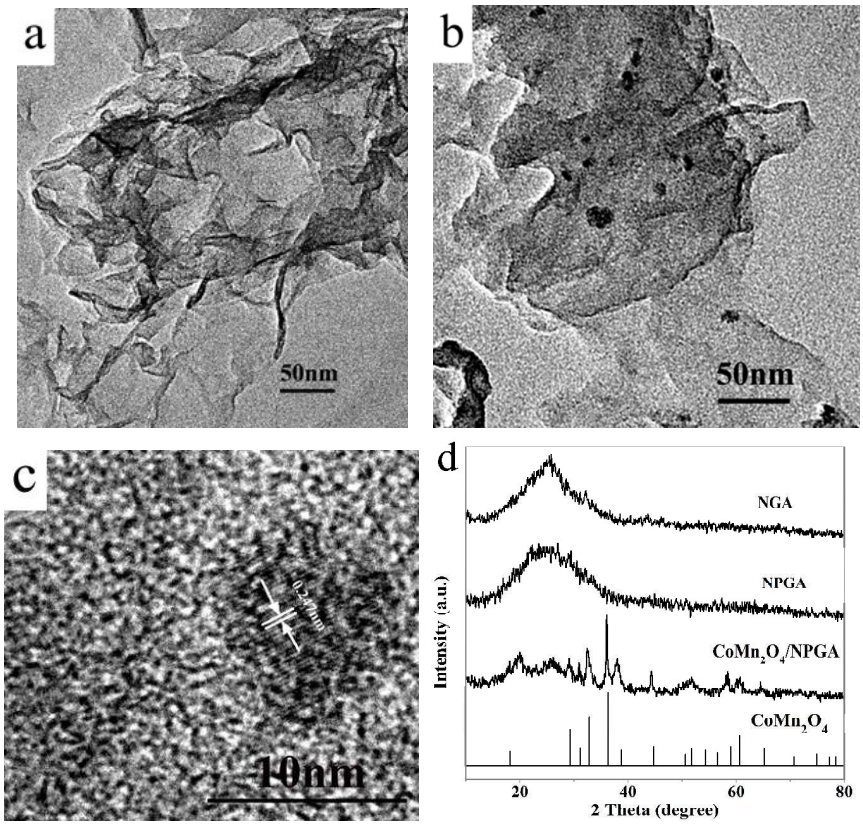

Fig. 2. TEM images of (a) NGA and (b) $CoMn_2O_4$/NPGA; (c) HRTEM images of the $CoMn_2O_4$/NPGA; (d) XRD patterns of NGA, NPGA, $CoMn_2O_4$/NPGA and JCPDS Card.

View Article Online
DOI: 10.1039/C6RA16337H

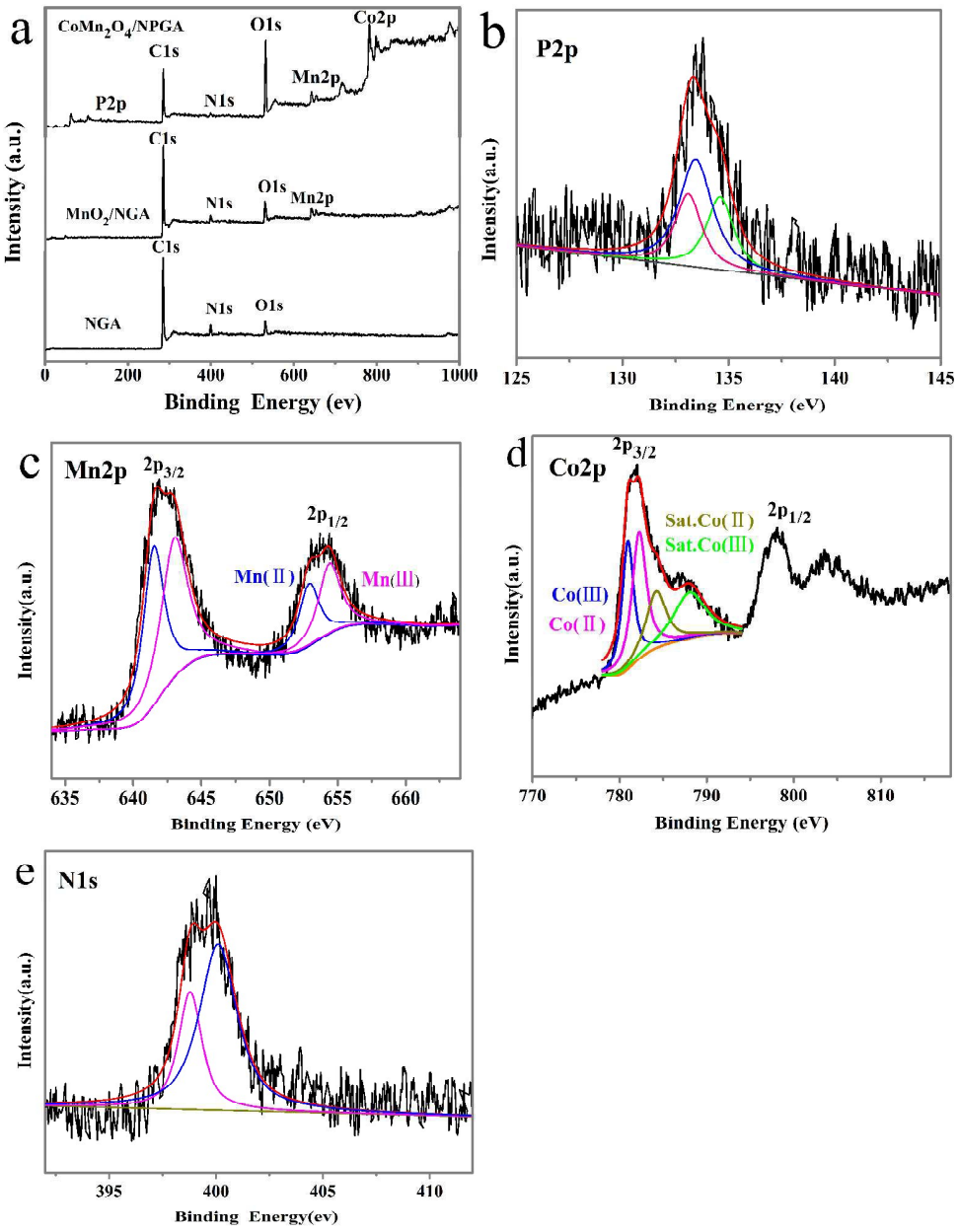

Fig. 3. (a) XPS spectra of NGA, MnO_2/NGA and $CoMn_2O_4$/NPGA composite; (b) high-resolution P2p XPS spectra of $CoMn_2O_4$/NPGA; (c) high-resolution Mn2p XPS spectra of $CoMn_2O_4$/NPGA; (d) high-resolution Co2p XPS spectra of $CoMn_2O_4$/NPGA; (e) high-resolution N1s XPS spectra of $CoMn_2O_4$/NPGA.

View Article Online
DOI: 10.1039/C6RA16337H

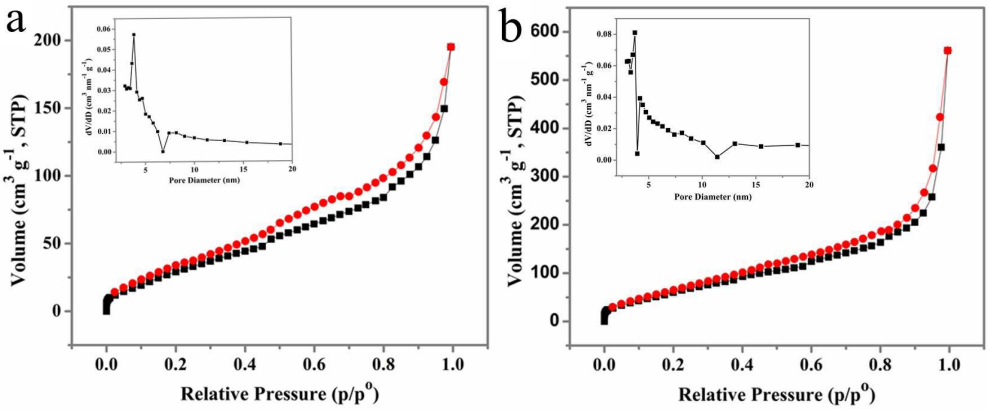

Fig. 4. Nitrogen adsorption−desorption isotherm and pore size distribution (inset) for $CoMn_2O_4$/NPGA (a) and NGA (b).

View Article Online
DOI: 10.1039/C6RA16337H

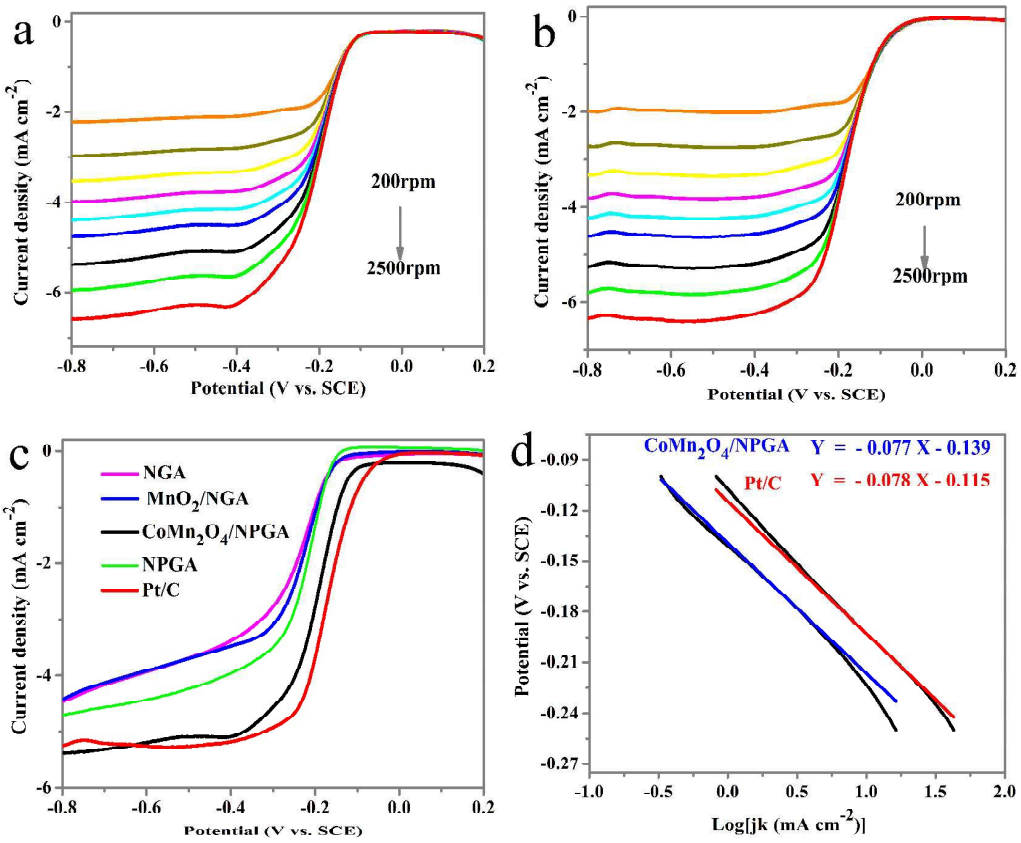

Fig. 5. LSV curves for ORR on (a) $CoMn_2O_4$/NPGA, (b) Pt/C at different rotation speeds from +0.2 to -0.8 V in O_2-saturated 0.1 M KOH with the scan rate of 10 mV s^{-1}; (c) LSV curves of the ORR on $CoMn_2O_4$/NPGA, MnO_2/NGA, NPGA, NGA and Pt/C at 1600 rpm in O_2-saturated 0.1 M KOH with the scan rate of 10 mV s^{-1}; (d) Tafel plots for the ORR on the $CoMn_2O_4$/NPGA and Pt/C in 0.1 M O_2-saturated KOH solution at a rotation rate of 1600 rpm.

View Article Online
DOI: 10.1039/C6RA16337H

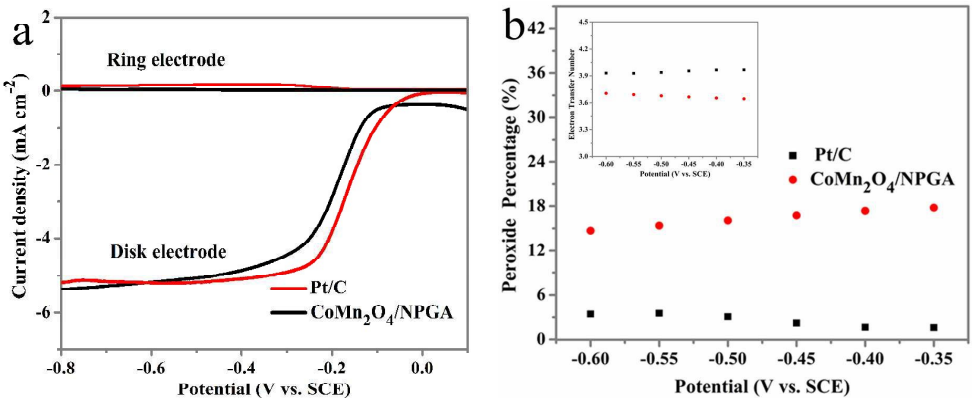

Fig. 6. (a) RRDE linear sweep voltammograms of the ORR on $CoMn_2O_4$/NPGA and Pt/C in O_2 -saturated 0.1 M KOH at a scan rate of 10 mV $s^{-1}$with a rotation speed of 1600 rpm. The ring electrode is polarized at 0.1 V vs. SCE; (b) Peroxide percentage and electron transfer number (inset) of $CoMn_2O_4$/NPGA and Pt/C at fixed potentials of -0.35, -0.4, -0.45, -0.5,-0.55 and -0.6 V vs. SCE.

View Article Online
DOI: 10.1039/C6RA16337H

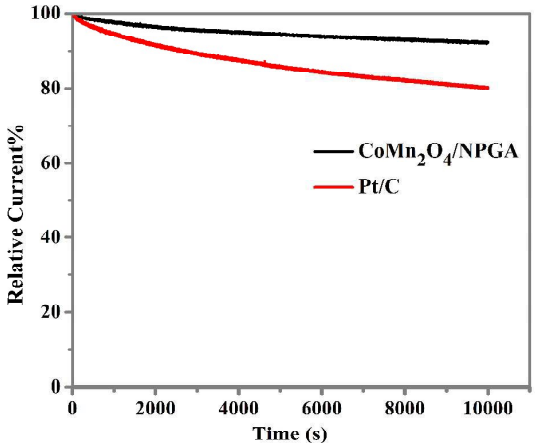

Figure. 7. Current−time (i−t) chronoamperometric responses of $CoMn_2O_4$/NPGA and commercial Pt/C catalysts at −0.4 V vs. SCE in O_2-saturated 0.1 M KOH solution with a rotation rate of 1600 rpm.

View Article Online
DOI: 10.1039/C6RA16337H

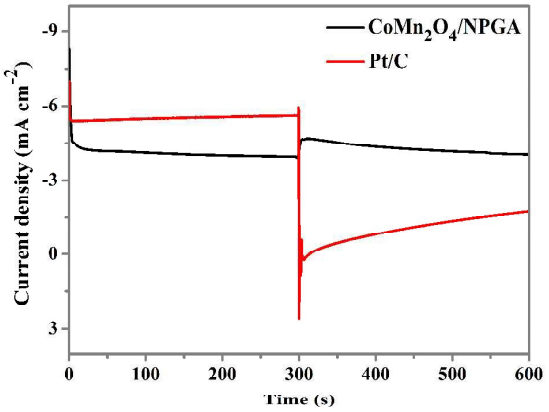

Figure. 8. Current−time (i−t) chronoamperometric for Pt/C and $CoMn_2O_4$/NPGA in O_2-saturated 0.1 M KOH solution and addition of 3 M methanol in 300 seconds.

View Article Online
DOI: 10.1039/C6RA16337H

Table

Table 1 Textural parameters of the NGA and $CoMn_2O_4$/NPGA

Sample	S_{BET} [a] ($m^2\ g^{-1}$)	S_{mes} [b] ($m^2\ g^{-1}$)	S_{mac} [c] ($m^2\ g^{-1}$)	PV [d] ($cm^3\ g^{-1}$)
NGA	276.0	190.9	85.1	0.87
$CoMn_2O_4$/NPGA	135.8	97.5	38.3	0.30

[a] Specific surface area from multiple BET method; [b] Micropore surface area from DFT method; [c] Macropore surface area ($S_{mac}=S_{BET}-S_{mes}$); [d] Total pore volume at $P/P^0=0.99$.

Table 2 electrochemical results for ORR estimated from LSV

Electrocatalysts	E_{onset} V *vs.* SCE	$E_{1/2}$ V *vs.* SCE	J_L (mA cm^{-2}) -0.8 V *vs.* SCE
$CoMn_2O_4$/NPGA	-0.094	-0.20	-5.39
MnO_2/NGA	-0.136	-0.24	-4.42
NGA	-0.147	-0.26	-4.47
NPGA	-0.142	-0.23	-4.71
Pt/C	-0.028	-0.17	-5.25

J_L: limiting current density at -0.8 V vs. SCE